Research Article

Scalable Van der Waals Two-Dimensional PtTe$_2$ Layers Integrated onto Silicon for Efficient Near-to-Mid Infrared Photodetection

Mashiyat Sumaiya Shawkat, Shihab Bin Hafiz, Molla Manjurul Islam, Sohrab Alex Mofid, Mohammad M. Al Mahfuz, Aritra Biswas, Hee-Suk Chung, Emmanuel Okogbue, Tae-Jun Ko, Debashis Chanda, Tania Roy,* Dong-Kyun Ko,* and Yeonwoong Jung*

Read Online

ACCESS | Metrics & More | Article Recommendations | Supporting Information

ABSTRACT: In recent years, there has been increasing interest in leveraging two-dimensional (2D) van der Waals (vdW) crystals for infrared (IR) photodetection, exploiting their unusual optoelectrical properties. Some 2D vdW materials with small band gap energies such as graphene and black phosphorus have been explored as stand-alone IR responsive layers in photodetectors. However, the devices incorporating these IR-sensitive 2D layers often exhibited poor performances owing to their preparation issues such as limited scalability and air instability. Herein, we explored wafer-scale 2D platinum ditelluride (PtTe$_2$) layers for near-to-mid IR photodetection by directly growing them onto silicon (Si) wafers. 2D PtTe$_2$/Si heterojunctions exhibited wavelength- and intensity-dependent high photocurrents in a spectral range of $\sim$1−7 μm, significantly outperforming stand-alone 2D PtTe$_2$ layers. The observed superiority is attributed to their excellent Schottky junction characteristics accompanying suppressed carrier recombination as well as optical absorbance competition between 2D PtTe$_2$ layers and Si. The direct and scalable growth of 2D PtTe$_2$ layers was further extended to demonstrate mechanically flexible IR photodetectors.

KEYWORDS: vdW crystal, 2D TMD layer, 2D PtTe$_2$, IR detection, photodetector
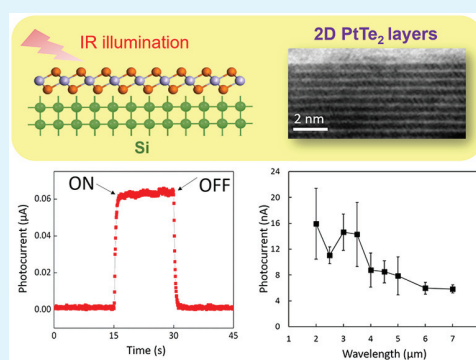
INTRODUCTION

Mid-infrared (MIR) radiation spans a vital part of the electromagnetic spectrum with special emphasis on spectroscopic applications employed for chemical analysis, military surveillance, and night vision.[1] The MIR-responsive active layers in current photodetectors are mostly based on thin-film or bulk materials composed of conventional three-dimensional (3D) compound semiconductors, for example, mercury cadmium telluride (MCT, HgCdTe alloys),[2] indium antimonide (InSb),[3] and their quantum-wells of complex structures and compositions.[4] However, their fabrication for MIR photodetectors to achieve desired performances are generally non-trivial. For instance, highly costly and sophisticated techniques (e.g., molecular beam epitaxy) are required to grow high-quality crystals, often entailing special conditions (e.g., cooling) for device operation.[5] Recently, two-dimensional (2D) materials have emerged as promising building blocks to alleviate these limitations owing to their rich set of unique properties; that is, tunable band gap energies covering a broad range of spectrum into MIR,[6,7] thickness-dependent tunable optical absorption,[8−10] decently high carrier mobility,[11,12] and relaxed assembly requirement benefiting from their weak van der Waals (vdW) bonding.[13,14] Additionally, the ultra-thin nature of 2D materials enables a low thermal noise, eliminating the strict requirement of device cooling. Some proof-of-concept methods utilizing graphene and 2D transition metal dichalcogenides (TMDs) have been demonstrated for photodetection in the MIR regime and beyond.[1,15−18] However, despite their intrinsic property advantages, these 2D materials are often limited to be employed as "stand-alone" active layers in MIR applications owing to their preparation issues. For example, while black phosphorus (BP) exhibits a small band gap energy of $\sim$0.3 eV and a high carrier mobility of $\sim$1000 cm^2 V^{-1} s^{-1} attractive for MIR detection, its poor air stability significantly limits resulting detection performance and reliability. Large-area graphene grown by a high temperature chemical vapor deposition (CVD) method generally requires an additional step of mechanical transfer and integration, severely limiting its process scalability. Similarly, conventional 2D TMD layers
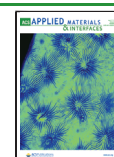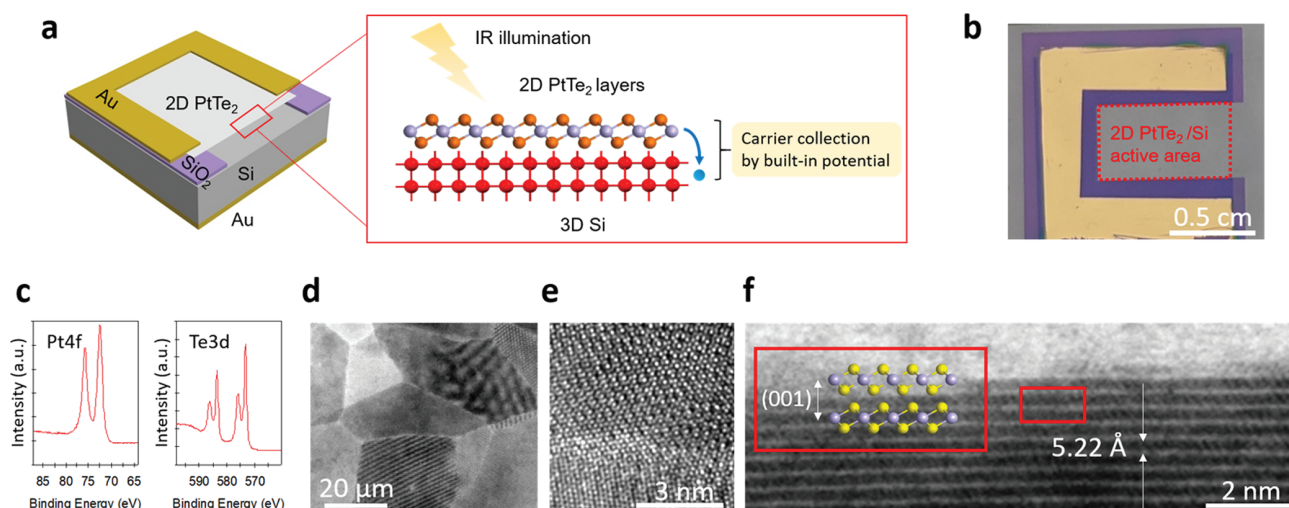
Figure 1. (a) Schematic illustration of a 2D PtTe$_2$/Si heterojunction device and its proposed working principle. (b) Camera image of a fabricated 2D PtTe$_2$/Si device. (c) XPS spectra of Pt 4f (left) and Te 3d (right) core levels obtained from 2D PtTe$_2$ layers grown on a Si wafer. (d) HR-STEM image demonstrating the poly-crystallinity of 2D PtTe$_2$ layers. (e) Bright-field HR-STEM revealing moiré fringes from two adjacent 2D layer grains. (f) Cross-sectional HR-STEM image of 2D PtTe$_2$ multilayers, showing an interlayer vdW gap spacing of ~5.22 Å.

employing refractory metals [e.g., molybdenum (Mo) or tungsten (W)] exhibit band gap energies matching the visible spectrum range and thus are less suitable for MIR detection compared to BP or graphene. Recently, there has been growing interest in "noble metals"-based 2D TMD layers which offer unparalleled properties such as small band gap energies matching the MIR range, low growth temperature, and high carrier mobility. Particularly, 2D platinum ditelluride (2D PtTe$_2$) layers exhibit ideal combination of various essential properties such as an extremely high electrical conductivity of >10^6 S/m[19−22] and a layer-number-dependent transition to a gapless metallic state.[12,23,24] A variety of preparation methods have been explored,[21,25,26] which have generally yielded randomly oriented small-sized 2D PtTe$_2$ flakes. A recently developed CVD method employing a thermal tellurization of Pt thin films enables their direct and deterministic growth on "wafer-scale" substrates even at a relatively low temperature of 400 °C.[20,22,27,28] This combined advantage of relaxed preparation requirement and superior material properties projects unprecedented opportunities of 2D PtTe$_2$ layers for MIR detection, which has remained largely unexplored till now.

Herein, we explore a new form of broadband MIR photodetectors by coupling 2D vdW-bonded PtTe$_2$ layers with 3D covalently bonded Si wafers through a CVD method. Even though stand-alone 2D PtTe$_2$ layers as well as Si wafers are not strongly MIR-sensitive, 2D PtTe$_2$/Si heterojunctions are observed to exhibit a significant amount of photoexcited carriers under MIR illumination measured up to ~7 μm in wavelength. The underlying working principle of these 2D/3D MIR photodetectors is discussed in the context of Schottky junction characteristics enabled by ultra-thin metallic 2D PtTe$_2$ layers interfaced with semiconducting Si as well as their optical absorbance competition.

■ RESULTS AND DISCUSSION

2D PtTe$_2$/Si MIR photodetectors are fabricated by a direct CVD growth of "wafer-scale" 2D PtTe$_2$ layers on top of p-type Si (1−5 Ω cm) wafers with pre-patterned SiO$_2$ areas. The

growth is performed at 400 °C by thermal tellurization of Pt seed films pre-deposited on the wafers. On the top side of the devices, 2D PtTe$_2$/Si areas function as active layers responsive to MIR illumination and 2D PtTe$_2$/SiO$_2$ areas are connected to the top gold (Au) electrodes. The back side of the Si wafers is connected to the bottom Au electrodes, ensuring the vertical 2D/3D heterojunction for electrical measurements. Details for the CVD growth of 2D PtTe$_2$ layers and device fabrication steps are introduced in the Method section. Figure 1a presents a schematic illustration of a 2D PtTe$_2$/Si MIR photodetector showing essential device components. Stand-alone 2D PtTe$_2$ layers are known to generate weak photocarriers upon IR illumination as previously reported,[29] while their carrier recombination significantly limits resulting IR responsivity, that is, ~20 μA/W under an illumination of 1.5 μm wavelength.[29] In the current approach, the 2D PtTe$_2$/Si heterojunction (red box in Figure 1a) imposes a strong built-in potential due to its Schottky characteristics, that is, metallic 2D PtTe$_2$ layers/semiconducting Si. A presence of this intrinsic Schottky junction facilitates efficient photocarrier separation and collection leading to improved MIR responsivity—to be verified in the next section. Figure 1b presents a camera image of a fabricated 2D PtTe$_2$/Si device with an active junction area of 0.5 cm^2, comparable to the schematic presented in Figure 1a. X-ray photoelectron spectroscopy (XPS) was employed to confirm the successful growth of 2D PtTe$_2$ layers on top of Si wafers. The XPS spectra in Figure 1c reveal core-energy level peaks of Pt 4f at 72.4 and 75.7 eV corresponding to 4f$_{7/2}$ and 4f$_{5/2}$, respectively, which is fully consistent with the previous reports on 2D PtTe$_2$ layers.[26,30] Also, Te 3d core-energy level peaks corresponding to the Te(IV) oxidation state appear at 576 and 586.3 eV, as well as additional peaks of Te(0) appearing at 573.3 and 583.4 eV. This observation is also consistent with previous studies,[30,31] further confirming the successful CVD growth of 2D PtTe$_2$ layers. Scanning transmission electron microscopy (STEM) was employed to identify the atomic structure of as-grown 2D PtTe$_2$ layers. Figure 1d presents a dark-field high-resolution STEM (HR-STEM) image of large-area 2D PtTe$_2$ layers, confirming their poly-crystalline structure manifested by well-defined crystalline
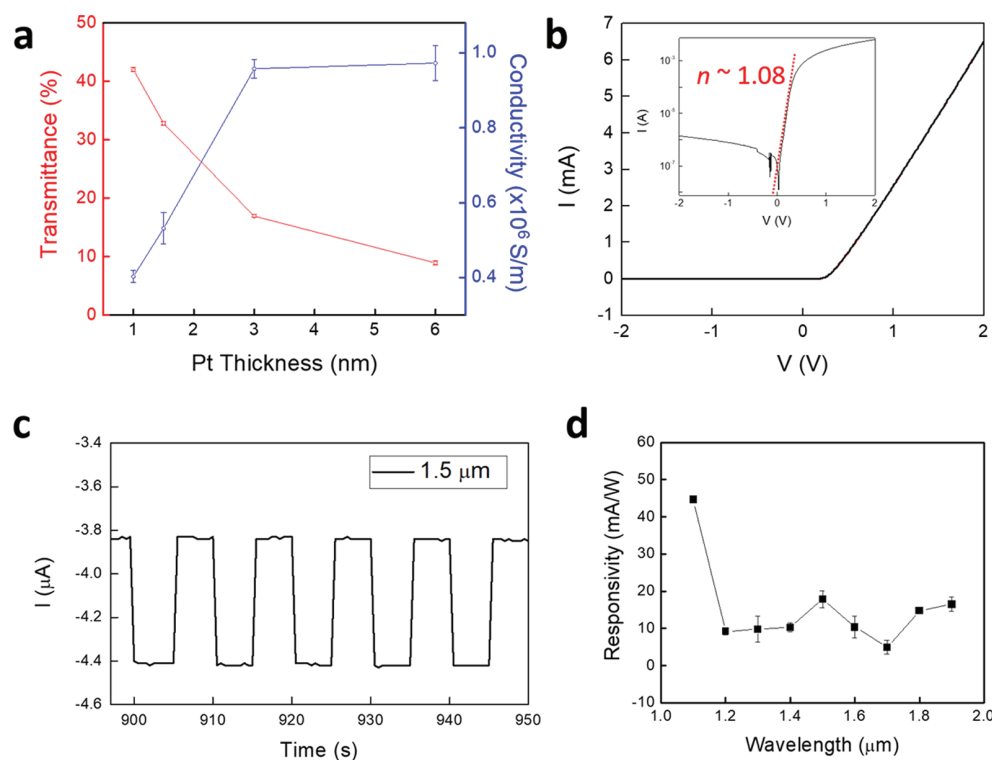
Figure 2. (a) Plot of optical transmittance (red) vs electrical conductivity (blue) for 2D PtTe$_2$ layers prepared with varying Pt thickness values. (b) I−V curve in dark and its corresponding semilog plot (inset) denoting an ideality factor of ~1.08. (c) Temporal photo-response of the same device in (b) under 1.5 μm illumination. (d) Illumination wavelength-dependent responsivity.

grains and their boundaries. Figure 1e shows an enlarged plane view of two adjacent grains in a bright field mode, revealing the presence of moiré fringes, which indicates vertical stacking of individual 2D layers of misaligned orientations. Figure 1f displays a cross-sectional HR-STEM image to visualize the vertical stacking of horizontally aligned individual 2D PtTe$_2$ layers with a well-resolved vdW gap spacing of ~5.22 Å corresponding to the (001) plane of a hexagonal 1T-PtTe$_2$ layered crystal.[25,26] The red box illustrates the atomic structure model of 2D PtTe$_2$ layers, showing that each Te−Pt−Te layer comprises an edge-connected octahedral configuration, as verified in our previous studies.[20]

Figure 2 presents key electrical and optical properties of 2D PtTe$_2$ layers as well as photodetection performances of 2D PtTe$_2$/Si heterojunction devices. Figure 2a presents the variation of optical transmittance and electrical conductivity of 2D PtTe$_2$ layers measured by an ultraviolet−visible (UV−vis) spectroscopy and a probe station, respectively. The plot reveals decreasing optical transmittance and increasing electrical conductivity with an increase of Pt seed thickness. Notably, 2D PtTe$_2$ layers are highly metallic, as confirmed in our previous studies,[28] reaching a high electrical conductivity of ~10^6 S/m.[20] We then explored intrinsic transport characteristics of 2D PtTe$_2$/Si devices and their photo-responsiveness under illumination. Figure 2b represents a two-terminal current−voltage (I−V) curve obtained from a representative device prepared with Pt of ~4.5 nm thickness. Highly asymmetric I−V characteristics are observed in dark, yielding a large rectification ratio of ~10^4 defined at ± 2 V. This strong rectification originates from a Schottky junction enabled by metallic 2D PtTe$_2$ layers interfaced with a semiconducting Si, as previously clarified.[28] We further

analyzed the I−V characteristics by employing a thermionic emission transport model. Within a forward bias regime of V > ~3kT/q, the current transport through a Schottky diode can be expressed as following.[32]

$$I \approx I_0 \ e^{V - IR_s/nkT/q} \tag{1}$$

$$I_0 \approx A \cdot A^{**} T^2 \ e^{-\Phi_B/kT} \tag{2}$$

where n, V, R_s, k, T, q, A, A^{**}, and Φ_B are the device ideality factor, bias voltage, series resistance, Boltzmann's constant, temperature, elementary charge, device active area, Richardson's constant, and Schottky barrier height, respectively. Excellent agreement is observed between the experimental versus modeled I−V characteristics with the Φ_B ~ 0.84 eV. The inset shows the corresponding semilog plot where a device ideality factor of ~1.08 is extracted from the linear fit (red dotted line) in the forward bias regime. This ideality factor being close to unity combined with the large rectification ratio indicates a high quality of the Schottky junction (i.e., minimal trap-assisted recombination in the depletion region). The photo-responsiveness of the device was first investigated at the near-infrared (NIR) regime ranging ~1.1−1.9 μm in wavelength. Figure 2c presents temporal photo-response obtained from the same device under a periodic NIR illumination of 1.5 μm in wavelength. The results confirm a significant generation of NIR-excited photocarriers, measured at a constant bias of −2 V under 0.1 mW/cm^2 intensity. One of the key performance metrics for photodetection is responsivity, which is defined as the ratio of the photocurrent to the optical power of incident radiation.[28] Figure 2d presents a plot of responsivity versus illumination wavelength in the NIR range of ~1.1−1.9 μm. The responsivity initially decreases
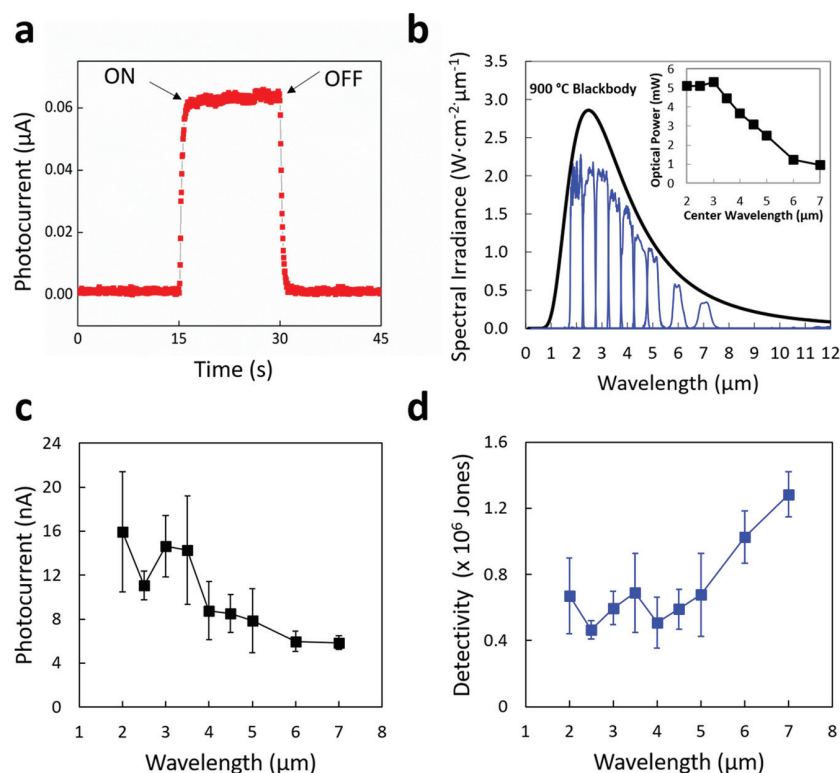
Figure 3. (a) Plot of MIR photocurrent measured using 900 °C-calibrated blackbody radiation filtered with Ge as an illumination source. (b) Spectral irradiance of the blackbody obtained from a band-pass filter in a center wavelength range of 2−7 μm, estimated using the Planck radiation formula. The inset displays the calculated optical power obtained by integrating the area under the respective blue curves at each wavelength. (c) Photocurrents measured with illumination of varying wavelengths. (d) Illumination wavelength-dependent specific detectivity. All measurements were conducted at room temperature 300 K using a constant bias of −0.6 V.

after ∼1.1 μm, possibly due to the significant absorbance reduction in Si,[33,34] and then it becomes nearly saturated beyond that wavelength. Interestingly, the responsivity is observed to be significantly larger than the values previously observed with stand-alone 2D PtTe$_2$ layers in the similar wavelength range; for instance, at a wavelength of 1.5 μm, the responsivity for the 2D PtTe$_2$/Si device is observed to be ∼13 mA/W. This value is approximately 1000 times larger than that from stand-alone 2D PtTe$_2$ layers at the same wavelength[29] despite the significantly larger (>10^{10} times) active area of the device. 2D materials can absorb IR radiation in a wide range of wavelengths through interband and/or intersubband transitions,[35,36] while precise electronic structures and transition mechanisms of 2D PtTe$_2$ layers need to be further investigated.

Photoexcited carriers can give rise to photocurrent if they are energetically positioned to overcome the Schottky barrier via thermionic or thermionic-field emission (typically, reverse-biased operation). The achievable cutoff wavelength of our 2D PtTe$_2$/Si Schottky diode is then predominantly determined by the height of the potential barrier. Analysis of the I−V characteristics (Figure 2b) reveals the presence of a Schottky junction with an appropriate barrier height enabling the device to generate photoexcited carriers even at longer wavelengths. Furthermore, a band structure diagram of the 2D PtTe$_2$/Si Schottky junction is proposed in the Supporting Information, Figure S1.

Figure 3a shows a representative plot of the temporal photocurrent measurement carried out by illuminating the device with MIR radiation with the photon wavelength longer than 2 μm. The radiation was provided by a calibrated

blackbody heated at 900 °C, which was then filtered through germanium (Ge) that only allowed mid- to long-IR radiation to pass through. A distinct increase in the photocurrent suggests that our device is indeed responsive in the thermal IR regimes. To further identify the photo-response characteristics, spectral photocurrent measurements were then carried out by replacing the Ge filter with various Fabry−Perot band-pass filters having a center wavelength in the ∼2−7 μm range, as shown in Figure 3b. Interestingly, an appreciable photocurrent was observed up to 7 μm even at room temperature (Figure 3c), although a large number of thermal carriers present at 300 K are expected to annihilate photogenerated carriers through the Auger recombination process, which typically necessitates device cooling.[37,38] The quality of a photodetector is evaluated with specific detectivity, D^*, a performance parameter defined by

$$D^* = \frac{R\sqrt{A\Delta f}}{I_n} \tag{3}$$

where A, Δf, I_n, and R are the device area, detection bandwidth, noise current, and responsivity, respectively.[39] Here, the optical power of the incident radiation for each specific filter was calculated based on the spectral irradiance of the calibrated blackbody estimated from the Planck radiation formula expressed as follows

$$P = A \cdot W \cdot \frac{a^2}{4d^2} \cdot t \cdot \eta \tag{4}$$
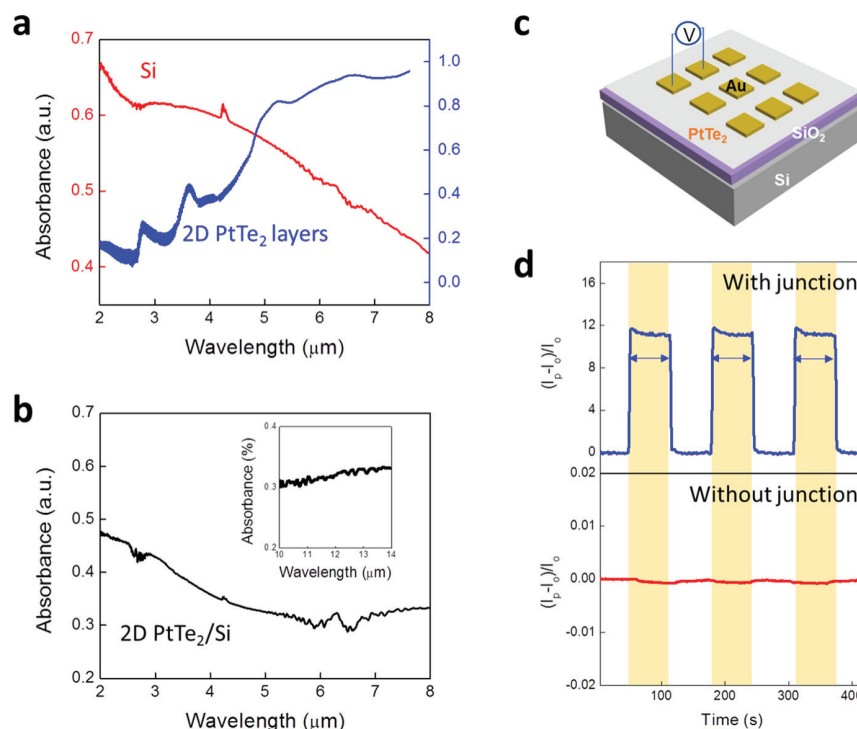
Figure 4. (a) FTIR absorbance spectra of a bare Si wafer (red) and 2D PtTe$_2$ layers integrated on a glass (blue). (b) FTIR absorbance spectrum of a 2D PtTe$_2$/Si device and the corresponding characteristics up to 14 μm in wavelength (inset). (c) Schematic illustration of a stand-alone 2D PtTe$_2$ layer-based device. (d) Temporal photo-response of devices with and without the 2D PtTe$_2$/Si junction. The device with the junction was characterized with an illumination frequency of 1000 Hz (blue arrow).

where A (0.5 cm^2), W, a (2.54 cm), d (13.5 cm), t (0.92), and η (1.33) are the device area, emittance of radiation for each specific filter, diameter of the source aperture, source aperture to device distance, transmission of the optical path, and amplification factor of the parabolic mirror, respectively. The inset in Figure 3b shows the calculated optical power at each center wavelength. With the measured noise current density of 3.3×10^{-12} A·Hz$^{-1/2}$ at 150 Hz, specific detectivity values were plotted as a function of wavelength, as shown in Figure 3d. While the device detectivity remains nearly constant in the low wavelength regime, it steadily increases beyond ~6 μm. The obtained specific detectivity values are on par with some of the earlier studies on various nanomaterials studied at the similar wavelength range.[40,41] Based on the observed trend, the cutoff wavelength of our 2D PtTe$_2$/Si device is believed to exist beyond the wavelength limit of the current optoelectronic measurement setup, that is, 7 μm, thus warranting further investigation.

To gain insights into the working principle of the observed wavelength-dependent detectivity, we performed Fourier transform IR (FTIR) spectroscopy characterization. Figure 4a presents absorbance spectra of a bare Si wafer as well as 2D PtTe$_2$ layers on a glass substrate. It is observed that the Si wafer displays decreasing absorbance with the increasing wavelength, while the 2D PtTe$_2$/glass sample exhibits the opposite characteristics. Furthermore, we performed FTIR characterization of a 2D PtTe$_2$/Si device, as presented in Figure 4b. Despite the continued decrease of absorbance in the Si wafer (Figure 4a), the device shows a slight increase in absorbance beyond ~6 μm in wavelength, which becomes continuously pronounced even with the longer wavelength (inset). This observation indicates that the decreasing

absorbance of the underlying Si wafer in the 2D PtTe$_2$/Si device is efficiently compensated by the increasing absorbance of 2D PtTe$_2$ layers. Accordingly, the overall absorbance of the device continuously increases after a certain critical wavelength, that is, ~6 μm, which possibly accounts for the wavelength-dependent increase of detectivity shown in Figure 3d. Furthermore, to better clarify an exclusive role of the 2D PtTe$_2$/Si Schottky junction in resulting IR photodetection, we performed a control experiment by exploring a device without the junction. Figure 4c shows a schematic illustration of the device where patterned 2D PtTe$_2$ layers are directly grown on a SiO$_2$/Si wafer, and their responsivity was evaluated by a two-terminal characterization under IR illumination. Figure 4d presents plots of temporal photo-response obtained from the devices with (top panel) and without (bottom panel) the Schottky junction, manifested by a photocurrent ratio, that is, $(I_p - I_o)/I_o$, where I_p is the IR-induced photocurrent and I_o is the dark current. The device without the junction corresponding to Figure 4c does not exhibit pronounced photocurrent in sharp contrast to the one with the junction, evidencing that the presence of the junction is essential for improved IR detection.

Lastly, we extend the scope of this study by exploring mechanically flexible IR photodetectors employing 2D PtTe$_2$ layers grown on thin (50 μm) Si wafers. Figure 5a demonstrates the mechanical flexibility of a thin Si wafer supported on a plastic substrate (top panel) and shows an image of a fabricated 2D PtTe$_2$/Si device (bottom panel). Figure 5b presents plots of temporal photo-response obtained from the corresponding device, represented as a photocurrent ratio of $(I_p - I_o)/I_o$. The results confirm illumination intensity-dependent photocurrent generation with well-defined responsiveness. Figure 5c shows a plot of photocurrent generation
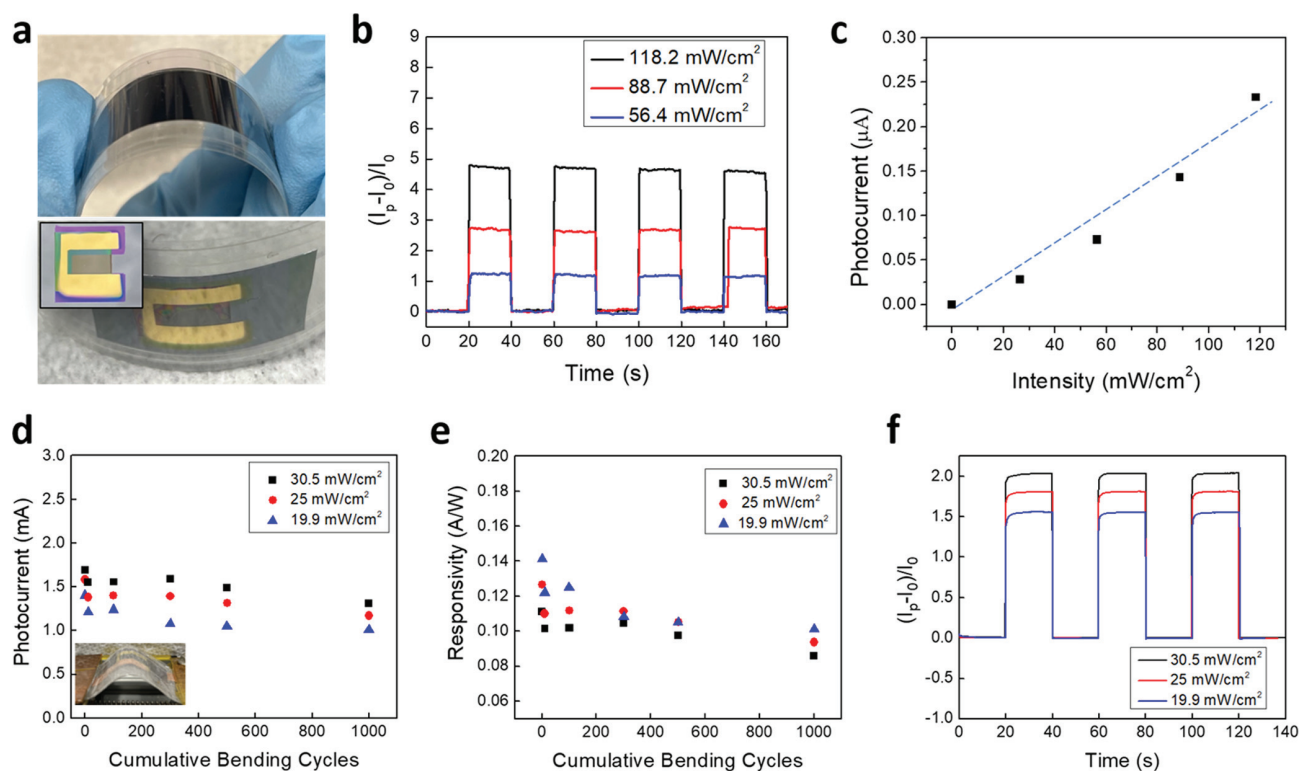
Figure 5. (a) Images of a thin Si wafer under bending (top) and a 2D PtTe$_2$/Si flexible photodetector (bottom). The inset shows the top view of the device prior to its attachment to the supporting substrate. (b) Intensity-dependent temporal photo-response obtained from the flexible 2D PtTe$_2$/Si device at an illumination wavelength of 0.94 μm. (c) Plot of photocurrent vs illumination intensity. (d) Plot of photocurrent vs bending cycles for a flexible device subjected to a reduction of lateral length by 20%. (e) Plot of responsivity vs bending cycles. (f) Plot of intensity-dependent temporal photo-response obtained after a completion of 1000 bending cycles.

versus illumination intensity showing high linearity, which suggests that the flexible device reliably responds to the illumination of varying intensities. Furthermore, mechano-optoelectrical properties of the flexible device were characterized by cyclic bending tests. The device was subjected to a sequential application of bending/unbending for a large number of cycles, where the bending degree was set to be a 20% reduction of its original lateral length. Figure 5d shows a plot of illumination intensity-dependent photocurrents with varying cycle numbers, and the insets shows a representative image of a device at its 20% bent state. Figure 5e shows a plot of illumination intensity-dependent responsivity corresponding to Figure 5d. After 1000 cycle numbers, only ~20 and ~27% reduction of photocurrent (Figure 5d) and responsivity (Figure 5e) are observed, respectively. Figure 5f presents a plot of intensity-dependent temporal photo-response after a completion of cumulative bending/unbending tests for 1000 cycles, confirming the reliable operation of the device.

CONCLUSIONS

In conclusion, we explored IR photodetection of 2D PtTe$_2$ layers directly integrated onto Si wafers. 2D PtTe$_2$/Si Schottky junctions exhibited excellent photo-responsiveness in a NIR-to-MIR spectral range of ~1−7 μm owing to the diminished carrier recombination manifested by their close-to-unity ideality factor. A wavelength-dependent increase of specific detectivity was observed beyond 5 μm, which was attributed to be the result of absorbance competition between 2D PtTe$_2$ layers versus Si. Furthermore, the low-temperature growth

nature of 2D PtTe$_2$ layers enabled us to create mechanically flexible photodetectors where the presence of 2D PtTe$_2$/Si Schottky junctions was identified to be critical for IR photodetection. This study is projected to greatly broaden the versatility of Si-based IR photodetectors by incorporating 2D materials in a simple and cost-efficient manner.

METHOD

2D PtTe$_2$/Si Device Fabrication. A bare p-type Si wafer was cleaned with acetone, isopropyl alcohol, and deionized water. 300 nm SiO$_2$ was subsequently deposited onto the Si wafer through a shadow mask, defining an uncovered area of 1 cm × 0.5 cm at a rate of 1 Å/s by electron-beam evaporation (Thermionics VE-100). A Pt film of 4.5 nm thickness was deposited through another shadow mask by the same evaporator at a rate of 0.05 Å/s as this thickness was identified to exhibit the best photodetection performance. The sample was placed in the middle of a quartz tube furnace which contained Te powder on the upstream side. The tube was purged with argon (Ar) gas and pumped down to a base pressure of ~1 mTorr. The furnace temperature was raised to 400 °C in 50 min, and the temperature was maintained for a dwell time of 50 min, followed by natural cooling. 100 sccm Ar gas was constantly flowed into the furnace throughout the entire reaction, maintaining an operation pressure of ~80 mTorr.

TEM and Raman Characterization. Microstructure analysis of 2D PtTe$_2$ layers was performed using JEOL ARM 200 F Cs-corrected TEM at an operation voltage of 200 kV.

For plane-view TEM sample preparation, the buffered oxide etchant was directly applied to SiO_2/Si wafers with as-grown 2D $PtTe_2$ layers, which became directly delaminated and transferred onto copper TEM grids. For Raman spectroscopy characterization, a Renishaw RM 1000B system with a laser source of 514 nm wavelength was used.

FTIR Characterization. The spectral characterization was performed with a setup comprising a microscope-coupled (Hyperion 1000, Bruker Optics Inc.) FTIR spectrometer (Vertex 80, Bruker Optics Inc.) The spectrometer is configured with a thermal source, a KBr beam splitter, and a liquid nitrogen-cooled MCT detector. The microscope can be configured for both transmission and reflection measurements. The measurements were performed using two different sets of objective lens separately, 2.4×, NA 0.07, CaF_2 objectives (0.3−8 μm), and 2.4×, NA 0.07, ZnSe objectives (6−16 μm), to measure the whole wavelength range of interest. Reflection and transmission spectra were measured and averaged 128 times, and each averaged measurement at the same location was performed twice for validation. Backgrounds were taken in air at room temperature under similar conditions at which the experiments were performed.

Transmittance and Conductivity Characterization. The optical transmittance of 2D $PtTe_2$ layers was characterized using UV−vis spectroscopy (Cary WinUV spectrophotometer) at 625 nm wavelength with the samples directly grown on optically transparent willow glasses. The electrical conductivity of 2D $PtTe_2$ layers was determined by a four-point resistivity probe (SP4, Signatone, USA) connected to a source meter (Keithley 2400, Keithley Instruments, USA). Average values of the transmittance and conductivity were determined from five different sets of measurements.

Room-Temperature Electrical and NIR (1.1−1.9 μm) Photodetection. All electrical measurements were performed with a home-built probe station using a HP 4156 A semiconductor parameter analyzer. Temporal photo-response characteristics of the heterojunction devices were analyzed using a home-built system composed of a light source, Newport (66885), and a monochromator, Cornerstone (130B).

MIR (2−8 μm) Photodetection. The photocurrent measurements were carried out using a calibrated blackbody (900 °C, Newport 67030) as an illumination source. An optical chopper was used to modulate the blackbody radiation at 150 Hz, and the modulated radiation was filtered through a Ge long-pass filter that cuts off photons with a wavelength shorter than 1.8 μm. The device signal was first amplified using SR570 and measured using a lock-in technique (SR830). For spectral photocurrent measurements (photocurrent vs wavelength), a set of Fabry−Perot band-pass filters with the center wavelength in a range of 2−7 μm were used instead of the Ge filter. The noise current density was measured using an SR760 spectrum analyzer at 150 Hz, coupled with an SR570 preamplifier. The preamplifier provided a low-noise voltage bias to the device. The noise voltage density ($V \cdot Hz^{-1/2}$) was measured directly using SR760 and converted to the noise current density ($A \cdot Hz^{-1/2}$) by multiplying the sensitivity of the preamplifier. The spectrum analyzer, preamplifier, and device were kept inside a Faraday cage and grounded to a common point to minimize external noise. The specific detectivity at each wavelength was calculated using the measured responsivity and noise current density values. The opto-electrical data were determined from three different sets of measurements and were averaged, obtaining the error bars.

■ ASSOCIATED CONTENT

Ⓢ Supporting Information

The Supporting Information is available free of charge at https://pubs.acs.org/doi/10.1021/acsami.1c03512.

Band structure model for the 2D $PtTe_2$/Si junction and the corresponding transport mechanism (PDF)

■ AUTHOR INFORMATION

Corresponding Authors

Tania Roy − NanoScience Technology Center, Department of Electrical and Computer Engineering, and Department of Materials Science and Engineering, University of Central Florida, Orlando, Florida 32826, United States; Ⓞ orcid.org/0000-0003-1131-8068; Email: Tania.Roy@ucf.edu

Dong-Kyun Ko − Department of Electrical and Computer Engineering, New Jersey Institute of Technology, Newark, New Jersey 07102, United States; Ⓞ orcid.org/0000-0003-1834-0241; Email: dong.k.ko@njit.edu

Yeonwoong Jung − NanoScience Technology Center, Department of Electrical and Computer Engineering, and Department of Materials Science and Engineering, University of Central Florida, Orlando, Florida 32826, United States; Ⓞ orcid.org/0000-0001-6042-5551; Email: Yeonwoong.Jung@ucf.edu

Authors

Mashiyat Sumaiya Shawkat − NanoScience Technology Center and Department of Electrical and Computer Engineering, University of Central Florida, Orlando, Florida 32826, United States; Ⓞ orcid.org/0000-0001-6594-190X

Shihab Bin Hafiz − Department of Electrical and Computer Engineering, New Jersey Institute of Technology, Newark, New Jersey 07102, United States

Molla Manjurul Islam − NanoScience Technology Center and Department of Physics, University of Central Florida, Orlando, Florida 32826, United States

Sohrab Alex Mofid − NanoScience Technology Center, University of Central Florida, Orlando, Florida 32826, United States

Mohammad M. Al Mahfuz − Department of Electrical and Computer Engineering, New Jersey Institute of Technology, Newark, New Jersey 07102, United States

Aritra Biswas − NanoScience Technology Center and The College of Optics and Photonics, University of Central Florida, Orlando, Florida 32826, United States

Hee-Suk Chung − Analytical Research Division, Korea Basic Science Institute, Jeonju 54907, South Korea

Emmanuel Okogbue − NanoScience Technology Center and Department of Electrical and Computer Engineering, University of Central Florida, Orlando, Florida 32826, United States

Tae-Jun Ko − NanoScience Technology Center, University of Central Florida, Orlando, Florida 32826, United States

Debashis Chanda − NanoScience Technology Center, Department of Physics, and The College of Optics and Photonics, University of Central Florida, Orlando, Florida 32826, United States

Complete contact information is available at:

Author Contributions

M.S.S. prepared 2D PtTe$_2$ layers, fabricated 2D PtTe$_2$/Si devices, and characterized their electrical properties under the guidance of Y.J. S.B.H. and M.M.A.M. performed the MIR measurements under the guidance of D.-K.K. M.M.I. performed the NIR measurements under the guidance of T.R. A.B. and S.A.M. performed the FTIR measurement under the guidance of D.C. E.O. and T.-J.K. performed the electrical conductivity and optical transmittance characterization under the guidance of Y.J. H.-S.C. performed the spectroscopy and TEM characterization of 2D PtTe$_2$ layers. M.S.S. wrote the manuscript with inputs from T.R., D.-K.K., and Y.J.

Notes

The authors declare no competing financial interest.

■ REFERENCES

(1) Fang, Y.; Ge, Y.; Wang, C.; Zhang, H. Mid-Infrared Photonics Using 2D Materials: Status and Challenges. *Laser Photonics Rev.* **2020**, *14*, 1900098.

(2) Rogalski, A. HgCdTe Infrared Detector Material: History, Status and Outlook. *Rep. Prog. Phys.* **2005**, *68*, 2267−2336.

(3) Xu, J.; Hu, J.; Wang, R.; Li, Q.; Li, W.; Guo, Y.; Liu, F.; Ullah, Z.; Wen, L.; Liu, L. Ultra-Broadband Graphene-InSb Heterojunction Photodetector. *Appl. Phys. Lett.* **2017**, *111*, 051106.

(4) Sarusi, G. QWIP or Other Alternative for Third Generation Infrared Systems. *Infrared Phys. Technol.* **2003**, *44*, 439−444.

(5) Wang, F.; Zhang, Y.; Gao, Y.; Luo, P.; Su, J.; Han, W.; Liu, K.; Li, H.; Zhai, T. 2D Metal Chalcogenides for IR Photodetection. *Small* **2019**, *15*, 1901347.

(6) Guan, X.; Yu, X.; Periyanagounder, D.; Benzigar, M. R.; Huang, J. K.; Lin, C. H.; Kim, J.; Singh, S.; Hu, L.; Liu, G.; Li, D.; He, J. H.; Yan, F.; Wang, Q. J.; Wu, T. Recent Progress in Short- to Long-Wave Infrared Photodetection Using 2D Materials and Heterostructures. *Adv. Opt. Mater.* **2021**, *9*, 2001708.

(7) Yu, X. C.; Wang, Q. J. 2D Materials Based Mid-Infrared and Terahertz Optoelectronics, *2019 Asia Communications and Photonics Conference (ACP), 2−5 Nov*, 2019; p 1.

(8) Chhowalla, M.; Shin, H. S.; Eda, G.; Li, L.-J.; Loh, K. P.; Zhang, H. The Chemistry of Two-Dimensional Layered Transition Metal Dichalcogenide Nanosheets. *Nat. Chem.* **2013**, *5*, 263−275.

(9) Mak, K. F.; Shan, J. Photonics and Optoelectronics of 2D Semiconductor Transition Metal Dichalcogenides. *Nat. Photonics* **2016**, *10*, 216−226.

(10) Shawkat, M. S.; Chung, H.-S.; Dev, D.; Das, S.; Roy, T.; Jung, Y. Two-Dimensional/Three-Dimensional Schottky Junction Photovoltaic Devices Realized by the Direct CVD Growth of vdW 2D PtSe$_2$ Layers on Silicon. *ACS Appl. Mater. Interfaces* **2019**, *11*, 27251−27258.

(11) Ciarrocchi, A.; Avsar, A.; Ovchinnikov, D.; Kis, A. Thickness-Modulated Metal-to-Semiconductor Transformation in a Transition Metal Dichalcogenide. *Nat. Commun.* **2018**, *9*, 919.

(12) Villaos, R. A. B.; Crisostomo, C. P.; Huang, Z.-Q.; Huang, S.-M.; Padama, A. A. B.; Albao, M. A.; Lin, H.; Chuang, F.-C. Thickness Dependent Electronic Properties of Pt Dichalcogenides. *npj 2D Mater. Appl.* **2019**, *3*, 2.

(13) Britnell, L.; Ribeiro, R. M.; Eckmann, A.; Jalil, R.; Belle, B. D.; Mishchenko, A.; Kim, Y. J.; Gorbachev, R. V.; Georgiou, T.; Morozov, S. V.; Grigorenko, A. N.; Geim, A. K.; Casiraghi, C.; Neto, A. H. C.; Novoselov, K. S. Strong Light-Matter Interactions in Heterostructures of Atomically Thin Films. *Science* **2013**, *340*, 1311.

(14) Geim, A. K.; Grigorieva, I. V. Van Der Waals Heterostructures. *Nature* **2013**, *499*, 419−425.

(15) Zhou, Y.; Zhang, M.; Guo, Z.; Miao, L.; Han, S.-T.; Wang, Z.; Zhang, X.; Zhang, H.; Peng, Z. Recent Advances in Black Phosphorus-Based Photonics, Electronics, Sensors and Energy Devices. *Mater. Horiz.* **2017**, *4*, 997−1019.

(16) Kim, K.; Choi, J.-Y.; Kim, T.; Cho, S.-H.; Chung, H.-J. A Role for Graphene in Silicon-Based Semiconductor Devices. *Nature* **2011**, *479*, 338−344.

(17) Novoselov, K. S.; Fal'ko, V. I.; Colombo, L.; Gellert, P. R.; Schwab, M. G.; Kim, K. A Roadmap for Graphene. *Nature* **2012**, *490*, 192−200.

(18) Xia, F.; Wang, H.; Xiao, D.; Dubey, M.; Ramasubramaniam, A. Two-Dimensional Material Nanophotonics. *Nat. Photonics* **2014**, *8*, 899−907.

(19) Fu, L.; Hu, D.; Mendes, R. G.; Rümmeli, M. H.; Dai, Q.; Wu, B.; Fu, L.; Liu, Y. Highly Organized Epitaxy of Dirac Semimetallic PtTe$_2$ Crystals with Extrahigh Conductivity and Visible Surface Plasmons at Edges. *ACS Nano* **2018**, *12*, 9405−9411.

(20) Wang, M.; Ko, T.-J.; Shawkat, M. S.; Han, S. S.; Okogbue, E.; Chung, H.-S.; Bae, T.-S.; Sattar, S.; Gil, J.; Noh, C.; Oh, K. H.; Jung, Y.; Larsson, J. A.; Jung, Y. Wafer-Scale Growth of 2D PtTe$_2$ with Layer Orientation Tunable High Electrical Conductivity and Superior Hydrophobicity. *ACS Appl. Mater. Interfaces* **2020**, *12*, 10839−10851.

(21) Ma, H.; Chen, P.; Li, B.; Li, J.; Ai, R.; Zhang, Z.; Sun, G.; Yao, K.; Lin, Z.; Zhao, B.; Wu, R.; Tang, X.; Duan, X.; Duan, X. Thickness-Tunable Synthesis of Ultrathin Type-II Dirac Semimetal PtTe$_2$ Single Crystals and Their Thickness-Dependent Electronic Properties. *Nano Lett.* **2018**, *18*, 3523−3529.

(22) Okogbue, E.; Ko, T.-J.; Han, S. S.; Shawkat, M. S.; Wang, M.; Chung, H.-S.; Oh, K. H.; Jung, Y. Wafer-Scale 2D PtTe$_2$ Layers for High-Efficiency Mechanically Flexible Electro-Thermal Smart Window Applications. *Nanoscale* **2020**, *12*, 10647−10655.

(23) Lin, M.-K.; Villaos, R. A. B.; Hlevyack, J. A.; Chen, P.; Liu, R.-Y.; Hsu, C.-H.; Avila, J.; Mo, S.-K.; Chuang, F.-C.; Chiang, T. C. Dimensionality-Mediated Semimetal-Semiconductor Transition in Ultrathin PtTe$_2$ Films. *Phys. Rev. Lett.* **2020**, *124*, 036402.

(24) Shawkat, M. S.; Gil, J.; Han, S. S.; Ko, T.-J.; Wang, M.; Dev, D.; Kwon, J.; Lee, G.-H.; Oh, K. H.; Chung, H.-S.; Roy, T.; Jung, Y.; Jung, Y. Thickness-Independent Semiconducting-to-Metallic Conversion in Wafer-Scale Two-Dimensional PtSe$_2$ Layers by Plasma-Driven Chalcogen Defect Engineering. *ACS Appl. Mater. Interfaces* **2020**, *12*, 14341−14351.

(25) Yan, M.; Huang, H.; Zhang, K.; Wang, E.; Yao, W.; Deng, K.; Wan, G.; Zhang, H.; Arita, M.; Yang, H.; Sun, Z.; Yao, H.; Wu, Y.; Fan, S.; Duan, W.; Zhou, S. Lorentz-Violating Type-II Dirac Fermions in Transition Metal Dichalcogenide PtTe$_2$. *Nat. Commun.* **2017**, *8*, 257.

(26) Hao, S.; Zeng, J.; Xu, T.; Cong, X.; Wang, C.; Wu, C.; Wang, Y.; Liu, X.; Cao, T.; Su, G.; Jia, L.; Wu, Z.; Lin, Q.; Zhang, L.; Yan, S.; Guo, M.; Wang, Z.; Tan, P.; Sun, L.; Ni, Z.; Liang, S.-J.; Cui, X.; Miao, F. Low-Temperature Eutectic Synthesis of PtTe$_2$ with Weak Antilocalization and Controlled Layer Thinning. *Adv. Funct. Mater.* **2018**, *28*, 1803746.

(27) Ko, T.-J.; Han, S. S.; Okogbue, E.; Shawkat, M. S.; Wang, M.; Ma, J.; Bae, T.-S.; Hafiz, S. B.; Ko, D.-K.; Chung, H.-S.; Oh, K. H.; Jung, Y. Wafer-Scale 2D PtTe$_2$ Layers-Enabled Kirigami Heaters with Superior Mechanical Stretchability and Electro-Thermal Responsiveness. *Appl. Mater. Today* **2020**, *20*, 100718.

(28) Shawkat, M. S.; Chowdhury, T. A.; Chung, H.-S.; Sattar, S.; Ko, T.-J.; Larsson, J. A.; Jung, Y. Large-Area 2D PtTe$_2$/Silicon Vertical-Junction Devices with Ultrafast and High-Sensitivity Photodetection and Photovoltaic Enhancement by Integrating Water Droplets. *Nanoscale* **2020**, *12*, 23116−23124.

(29) Lai, J.; Ma, J.; Liu, Y.; Zhang, K.; Zhuo, X.; Chen, J.; Zhou, S.; Sun, D. Photocurrent Response of Type-II Dirac Semimetal PtTe$_2$. *2D Materials* **2020**, *7*, 034003.

(30) Politano, A.; Chiarello, G.; Kuo, C.-N.; Lue, C. S.; Edla, R.; Torelli, P.; Pellegrini, V.; Boukhvalov, D. W. Tailoring the Surface Chemical Reactivity of Transition-Metal Dichalcogenide PtTe$_2$ Crystals. *Adv. Funct. Mater.* **2018**, *28*, 1706504.

(31) Yang, S.; Cai, H.; Chen, B.; Ko, C.; Özçelik, V. O.; Ogletree, D. F.; White, C. E.; Shen, Y.; Tongay, S. Environmental Stability of 2D Anisotropic Tellurium Containing Nanomaterials: Anisotropic to Isotropic Transition. *Nanoscale* **2017**, *9*, 12288−12294.

(32) Ahmed, K.; Chiang, T. Schottky Barrier Height Extraction from Forward Current-Voltage Characteristics of Non-Ideal Diodes with High Series Resistance. *Appl. Phys. Lett.* **2013**, *102*, 042110.

(33) Xie, C.; Zeng, L.; Zhang, Z.; Tsang, Y.-H.; Luo, L.; Lee, J.-H. High-Performance Broadband Heterojunction Photodetectors Based on Multilayered PtSe$_2$ Directly Grown on a Si Substrate. *Nanoscale* **2018**, *10*, 15285−15293.

(34) Zeng, L.; Lin, S.; Lou, Z.; Yuan, H.; Long, H.; Li, Y.; Lu, W.; Lau, S. P.; Wu, D.; Tsang, Y. H. Ultrafast and Sensitive Photodetector Based on a PtSe$_2$/Silicon Nanowire Array Heterojunction with a Multiband Spectral Response from 200 to 1550 nm. *NPG Asia Mater.* **2018**, *10*, 352−362.

(35) Dawlaty, J. M.; Shivaraman, S.; Strait, J.; George, P.; Chandrashekhar, M.; Rana, F.; Spencer, M. G.; Veksler, D.; Chen, Y. Measurement of the Optical Absorption Spectra of Epitaxial Graphene from Terahertz to Visible. *Appl. Phys. Lett.* **2008**, *93*, 131905.

(36) Sensale-Rodriguez, B.; Yan, R.; Zhu, M.; Jena, D.; Liu, L.; Grace Xing, H. Efficient Terahertz Electro-Absorption Modulation Employing Graphene Plasmonic Structures. *Appl. Phys. Lett.* **2012**, *101*, 261115.

(37) Martyniuk, P.; Rogalski, A. Hot Infrared Photodetectors. *Opto-Electron. Rev.* **2013**, *21*, 239−257.

(38) Downs, C.; Vandervelde, T. Progress in Infrared Photo-detectors Since 2000. *Sensors* **2013**, *13*, 5054−5098.

(39) Dereniak, E.; Boreman, G. *Infrared Detectors and Systems*; Wiley: New York, 1996.

(40) Lai, J.; Liu, X.; Ma, J.; Wang, Q.; Zhang, K.; Ren, X.; Liu, Y.; Gu, Q.; Zhuo, X.; Lu, W.; Wu, Y.; Li, Y.; Feng, J.; Zhou, S.; Chen, J.-H.; Sun, D. Anisotropic Broadband Photoresponse of Layered Type-II Weyl Semimetal MoTe$_2$. *Adv. Mater.* **2018**, *30*, 1707152.

(41) Tang, X.; Ackerman, M. M.; Chen, M.; Guyot-Sionnest, P. Dual-Band Infrared Imaging Using Stacked Colloidal Quantum Dot Photodiodes. *Nat. Photonics* **2019**, *13*, 277−282.